A116 Vol. 41, No. 2 / February 2024 / Journal of the Optical Society of America B

Research Article

Journal of the Optical Society of America B

OPTICAL PHYSICS

Optimizing bi-layered periodic structures: a closed-form transfer matrix method based on Pendry-MacKinnon's discrete Maxwell's equations

Ovidiu-Zeno Lipan[1,*] and Aldo De Sabata[2]

[1]Department of Physics, 138 UR Drive, University of Richmond, Richmond, Virginia 23173, USA
[2]Department of Measurements and Optical Electronics, Politehnica University of Timisoara, 300006 Timisoara, Romania
*olipan@richmond.edu

Received 6 June 2023; revised 10 December 2023; accepted 8 January 2024; posted 12 January 2024; published 29 January 2024

The optimization procedure that we present is based on a closed-form exact analytical solution for the three-dimensional transfer matrix that we put forward in arXiv, arXiv:2303.06765 (2023). The analytical solution is valid for all modes, either propagative or evanescent, and any non-magnetic isotropic pattern with frequency-dependent permittivities. In this paper we exemplify the use of the transfer matrix elements to optimize a patterned bilaminar structure such that a subset of evanescent Bloch-Floquet modes $(M_x, M_y) \neq 0$ acquire large scattering matrix elements at a specified frequency. Such an excited resonant mode propagates along the device's surface at a frequency smaller than its Rayleigh frequency. These predictions are grouped into three categories. The first category, inspired by topological photonics, is related to robustness of the resonant modes with respect to the change of the dielectric constants, quantified as a map from the real to integer numbers. The second is based on resonant frequency identification, whereas the third is focused on high Q-factors and the use of a complex frequency plane to estimate the Fano-Lorentz spectral line shape for the resonant modes. All the predictions based on the proposed optimization were confirmed by a high-performance analysis software package [CST Studio Suite (2022)].

https://doi.org/10.1364/JOSAB.497185

1. INTRODUCTION

Thin stacks of layers can control electromagnetic fields to enable a variety of applications in the form of waveguides for augmented reality [1,2], frequency-selective surfaces for 5 and 6G networks [3], wearable applications [4], and surface wave-mediated sensing applications [5,6]. Optimization methods like evolutionary and combinatorial methods [7,8] have motivated a large number of design approaches. Some optimization methods are NP-hard, and so it is important to have theoretical results that can help to narrow down the search space. To this end, we are employing the transfer matrix method [9–17], which relates the fields from the input to the output of thin stacks of in-plane structured laminae. We prefer to use the term "structured laminae," because it more reflects the concepts we are referring to. The term "laminae" aptly captures the concept of the discrete theoretical model we use, which is based on an arrangement of parallel planes with no thickness. A lamina consists of a plane together with the narrow void that separates it from the neighboring plane. Moreover, each plane exhibits a structured composition, characteristic of an engineered material. Its unique characteristics arise from the deliberate inclusion of artificial structures within a uniform host medium. To utilize the theoretical model for a practical stack of thin non-homogeneous layers, we posit that the layer's structure is positioned on the lamina's plane, and the layer's thickness coincides with the thickness of the narrow void between it and the next plane.

A key motivation for writing this manuscript is that in a world increasingly dominated by data and algorithms, the insight of closed-form formulas remains a source of inspiration. By revealing the functional relationships between parameters and outcomes, closed-form solutions provide deeper insights into the system's behavior. This deeper understanding, in turn, facilitates further analysis, prediction, and design optimization.

The closed-form exact analytical solution that we developed in [18], being expressed in terms of familiar physical concepts, allows for the study of the factors that influence the optimization result. This paper highlights a subtle distinction between the transfer matrix method, viewed as a general concept, and transfer matrix formulas. Specifically, the transfer matrix method encompasses a broader, more general approach, while the transfer matrix formulas emphasize the derivation of closed-form

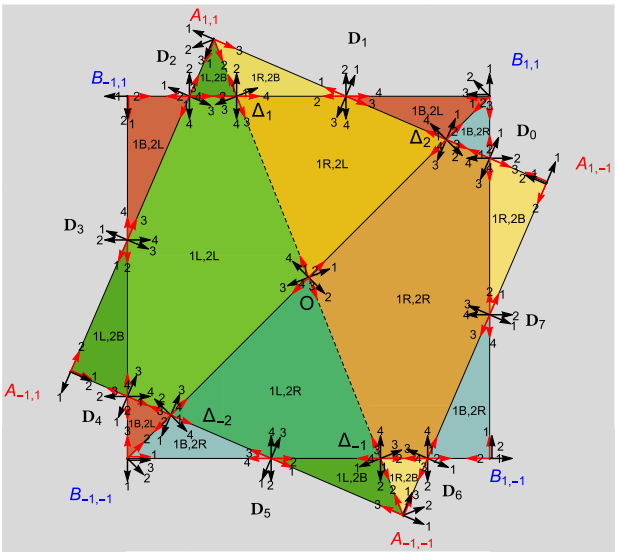

Fig. 1. π-π-rig pattern. The black arrows represent the $\hat{\lambda}$-vectors, whereas the red arrows represent the $\hat{\mu}$-vectors. The permittivity ϵ_{1L} is printed on the left triangle ($A_{1,1}$, $A_{-1,1}$, $A_{-1,-1}$), whereas ϵ_{1R} on the right triangle ($A_{1,-1}$, $A_{1,1}$, $A_{-1,-1}$), both on lamina 1. Same goes for lamina 2 where ϵ_{2L} and ϵ_{2R} label the left and right triangles with respect to the diagonal $B_{-1,-1}B_{1,1}$. Outside the interior squares, and up to the boundaries of the unit cell, the background permittivity ϵ_{1B} is printed on lamina 1 and ϵ_{2B} on lamina 2. The color and label of each polygon express the decomposition of the unit cell in polygons that carry a constant value of the product $\epsilon_1\epsilon_2$. The unit cell corners, which are not represented, have their own $(\hat{\lambda}, \hat{\mu})$-pairs.

analytical solutions for the matrix elements. This unique focus underscores the significance of closed-form solutions within the context of the transfer matrix method.

The transfer matrix strongly depends on the thickness of the laminae, which we consider to be analogous to a lattice constant. This motivated us in [18] to consider Maxwell's equations on a discrete space. Pendry and MacKinnon obtained a meaningful discretization of Maxwell's equations [19] on a carefully chosen simple cubic lattice [20] by retaining essential properties of the longitudinal modes present in the continuum. This discretization was put forward specifically as part of a finite-element numerical algorithm [21].

In this paper, which is the optimization-driven section of [18], we propose an optimization procedure for creating a dielectric bilaminar (made up of two laminae) structure, Fig. 1, on which a selected group of Bloch-Floquet modes propagates along the laminae with large amplitudes, being evanescent in the z-direction [22]. These resonances display a series of relevant properties. One, covered in Section 5, is the robustness with respect to the change of the dielectric constants. The resonant frequencies are located close to the zeroes of the diagonal elements of the transfer matrix. As the dielectric permittivities pass through different values, the zeroes are created or disappear allowing us to define a topological map that counts the number of resonant modes, Fig. 4.

In Sections 6 and 7 we find that the same bilaminar structure, but with specifically selected dielectric constants, resonates with a very large Q-factor, Fig. 13. Finally, in Section 8, the complete analytical formula, applied on the optimized result, offers the possibility to obtain the Fano-Lorentz spectral line shape for a resonant mode, [23,24], through a zero-pole approximation, Eq. (13), in the complex frequency plane, Fig. 15.

All the predictions based on the proposed optimization were confirmed by a high-performance analysis software package [25].

2. DEVICE DESCRIPTION

The optimization procedure is applied to the bilaminar pattern in Fig. 1, which we will call π-π-rig. The locations of the two laminae are described in the caption to Fig. 1. The thickness of each lamina is denoted by c. The unit cell is a square with corners positioned at $(\pm\pi, \pm\pi)$, in length units chosen for a desired frequency band. Inside the unit cell of each lamina sits an inner square. Figure 1 shows two inner squares, as expected for a bilaminar device. The corners of the unit cell are not visible in Fig. 1 to save the space for the information pertaining to the inner squares. In the foreground, the square has its vertices labeled $B_{i,j}$, $i = \pm 1$, $j = \pm 1$ positioned at $(\pm\pi/2, \pm\pi/2)$. In the background, the square with vertices $A_{i,j}$ is rotated counterclockwise by an angle α. For $\alpha = 0$, the squares' vertices coincide.

The separate dielectric patterns from the two layers create a polygonal tessellation in the x-y plane, defined by regions of constant value of the product $\epsilon_1\epsilon_2$. The $\hat{z}$-axis is coming out from the figure's page and $\hat{x}$ is oriented from $B_{-1,-1}$ to $B_{1,-1}$.

All vertices of the tessellation have associated with them a set of pairs of unit vectors, $(\hat{\lambda}, \hat{\mu})$. The tails of the $\hat{\mu}$ vectors are located at the vertices of the polygons, and they extend along the edges. From the same vertex, and associated to each $\hat{\mu}$, originates another unit vector $\hat{\lambda}$ in such a way that each pair $(\hat{\lambda}, \hat{\mu})$ is orthogonal and each triplet $(\hat{\lambda}, \hat{\mu}, \hat{z})$ is right-oriented.

Take for example the origin O. There are four segments that originate at O. One is the segment $OA_{1,1}$, which carries a unit vector denoted $\hat{\mu}_1$ in Fig. 1. Then $\hat{\mu}_2$, $\hat{\mu}_3$, and $\hat{\mu}_4$ are along $OB_{1,1}$, $OA_{-1,-1}$, and $OB_{-1,-1}$, respectively. All tails of these unit vectors sit on point O. From the same point O originates the another set of four unit vectors $\hat{\lambda}_i$, $i = 1, \ldots, 4$. The last geometrical parameter is related to the choice of a frequency band, say in GHz or THz, which scales the device's units to mm or μm, respectively. Versus this unit of length we define a unitless thickness parameter t:

$$t = [1\ \text{unit}](c\ [\text{unit}])^{-1}. \tag{1}$$

The frequency, the wavelength, and all (x, y) geometrical distances that appear in the transfer matrix formulas are c-scaled. For example, the c-scaled wavelength and frequency are $\lambda' = t\frac{\lambda\ [\text{unit}]}{1\ [\text{unit}]}$ and $\Omega = 2\pi\lambda'^{-1}$, respectively.

The geometrical data needed to compute the transfer matrix for any polygonal tessellation consists of the coordinates of all points, the orientations of all unit vectors, and a choice of the thickness parameter. The other kind of data comes from the permittivity jumps across polygonal segments. For example, for point O in Fig. 1 the relative permittivity pair $(\epsilon_{1R}, \epsilon_{2L})$ and $(\epsilon_{1L}, \epsilon_{2L})$ appears on the right-side and on the left-side looking along $\hat{\mu}_1$, respectively. As we cross $\hat{\mu}_1$ walking in the direction of $\hat{\lambda}_1$, slightly above point O, the change in relative permittivity

introduces a jump that is a key ingredient in the transfer matrix formulas.

3. TRANSFER MATRIX ELEMENTS

In this section, we present the essential information needed to understand the construction of the objective function. The transfer matrix elements we compute connect the IN electromagnetic field from the (x, y)-plane located $c/2$ below lamina A to the OUT field located $c/2$ above lamina B, along the $\hat{z}$-axis.

We use a plane wave basis $\psi^{\mathrm{DIR}}_{\mathrm{POL,BF}}$, which is described by three indices. The first, POL, is the polarization index, which takes two values S and P. The second, DIR, is the direction of propagation of the plane wave along the z-axis, which also take two values, $+$ and $-$. The third, BF, is the Bloch-Floquet index consisting of pairs of integer numbers (M_x, M_y). The direction of the incoming mode $(M_x = 0, M_y = 0)$ is stated in spherical coordinates by the angles (θ, φ).

The transfer matrix elements are defined in Eq. (2) as the factors that connect the coefficients of the IN and OUT fields decomposed in the reference medium plane wave basis:

$$C^{\mathrm{DIR}}_{\mathrm{POL,BF}} = \sum \left(T^{\mathrm{DIR;dir}}_{\mathrm{POL,BF;pol,bf}} \right) C^{\mathrm{dir}}_{\mathrm{pol,bf}}, \tag{2}$$

the sum being over indices (dir,pol,bf) related to the IN parameters.

Building a matrix out of the T-coefficients of Eq. (2) requires a map from the two-dimensional Bloch-Floquet index (M_x, M_y) to a one-dimensional integer index $m = 1, 2, \ldots, \infty$. We use the Rayleigh frequency of (M_x, M_y) to both map and order the Bloch-Floquet index. The Rayleigh frequency is regarded as the cut-off frequency of the transfer function of the free space. If the Rayleigh frequency of (M_x, M_y) is less than the Rayleigh frequency of (M'_x, M'_y) we order the Bloch-Floquet indices as $(M_x, M_y) < (M'_x, M'_y)$. If two distinct Bloch-Floquet modes have the same Rayleigh frequency, the order used is the lexicographic order. Note that this ordering depends on angles (θ, φ). The mode $(M_x, M_y) = (0, 0)$ has $f_{\mathrm{Rayleigh}} = 0$ and it is mapped into $m = 1$. The next $f_{\mathrm{Rayleigh}} > 0$ is mapped into $m = 2$ and so on.

Our work was completed before the feature announcement on Inverse Design in Photonics, so in Table 1 and for the rest of the paper the unit cell dimensions are in cm. That will place the resonant frequencies in the GHz domain where fabrication of 3D photonic crystals is more accessible. However, since the device is all-dielectric, the dimensions can be scaled for the THz domain.

The process of building the transfer matrix out of its elements starts with all 2×2 matrices,

$$T^{-,-}_{m,n} = \begin{pmatrix} T^{-,-}_{Sm,Sn} & T^{-,-}_{Sm,Pn} \\ T^{-,-}_{Pm,Sn} & T^{-,-}_{Pm,Pn} \end{pmatrix}, \tag{3}$$

constructed for each pair (m, n). These matrices contain the information about the transfer, through the device, of the mode n with a negative direction present at IN into the mode m, also with a negative direction but located at OUT.

From these 2×2-matrices, construct the transfer matrix $T^{-,-}$ using the Bloch-Floquet indices m and n:

$$T^{-,-} = \begin{pmatrix} T^{-,-}_{1,1} & T^{-,-}_{1,2} & T^{-,-}_{1,3} & \cdots \\ T^{-,-}_{2,1} & T^{-,-}_{2,2} & T^{-,-}_{2,3} & \cdots \\ T^{-,-}_{3,1} & T^{-,-}_{3,2} & T^{-,-}_{3,3} & \cdots \\ \cdots & \cdots & \cdots & \cdots \end{pmatrix}. \tag{4}$$

Once all four matrices $T^{-,-}$, $T^{-,+}$, $T^{+,-}$, $T^{+,+}$ are constructed in a similar manner, the complete transfer matrix appears as

$$T = \begin{pmatrix} T^{+,+} & T^{+,-} \\ T^{-,+} & T^{-,-} \end{pmatrix}. \tag{5}$$

The elements of the scattering matrix can now be obtained from the complete transfer matrix. The input and output have a different meaning for the scattering matrix than OUT and IN have for the transfer matrix. Instead of "DIR/dir," for the scattering matrix we use a position index, which is either min or max depending on the position on the z-axis of the field at $z = \mathrm{IN}$ or at $z = \mathrm{OUT}$, respectively. The polarization and the Bloch-Floquet indices remain the same.

The well-known procedure to obtain the scattering matrix [20],

$$t(\xi_x, \xi_y) = \begin{pmatrix} t^{\mathrm{max,min}} & t^{\mathrm{max,max}} \\ t^{\mathrm{min,min}} & t^{\mathrm{min,max}} \end{pmatrix}, \tag{6}$$

requires the inverse of the transfer matrix $T^{-,-}$:

$$t^{\mathrm{min,max}} = (T^{-,-})^{-1}, \tag{7}$$

$$t^{\mathrm{min,min}} = -t^{\mathrm{min,max}} T^{-,+}, \tag{8}$$

Table 1. Mode Ordering and Rayleigh Frequency for $\theta = 17.5°$ and $\varphi = 0°$

(M_x, M_y)	m	Pol., m	f_R [GHz]
(0,0)	1	$S1 = S(0, 0),\ P1 = P(0, 0)$	0.0
(−1,0)	2	$S2 = S(-1, 0),\ P2 = P(-1, 0)$	36.6827
(0,−1)	3	$S3 = S(0, -1),\ P3 = P(0, -1)$	50.0289
(0,1)	4	$S4 = S(0, 1),\ P4 = P(0, 1)$	50.0289
(−1,−1)	5	$S5 = S(-1, -1),\ P5 = P(-1, -1)$	56.7146
(−1,1)	6	$S6 = S(-1, 1),\ P6 = P(-1, 1)$	56.7146
(1,0)	7	$S7 = S(1, 0),\ P7 = P(1, 0)$	68.23087
(−2,0)	8	$S8 = S(-2, 0),\ P8 = P(-2, 0)$	73.36548
(−2,−1)	9	$S9 = S(-2, -1),\ P9 = P(-2, -1)$	84.68336
(−2,1)	10	$S10 = S(-2, 1),\ P10 = P(-2, 1)$	84.68336

$$t^{\max,\max} = T^{+,-} t^{\min,\max}, \tag{9}$$

$$t^{\max,\min} = T^{+,+} + t^{\max,\max} T^{-,-} t^{\min,\min}. \tag{10}$$

4. OPTIMIZATION PROCEDURE FOR SELECTING THE DIELECTRIC CONSTANTS

We design-optimize a dielectric structure from Fig. 1 such that a subset of evanescent Bloch-Floquet modes $(M_x, M_y) \neq 0$ acquires large scattering matrix elements at a specified frequency. Such an excited resonant mode propagates along the plane (x, y) at a frequency smaller than its Rayleigh frequency. Specifically, in the frequency range under study, 37–50 GHz, the optimization function is based on four modes. Two modes, (0, 0) and (−1, 0), propagate, and two other modes, (0, ±1), are evanescent, Table 1. The goal is to find a set of dielectric constants for which the modes (0, ±1) resonate. To excite the resonant modes, the plane wave (0, 0) coming from $z < 0$ lands at angles $\theta = 17.5°$ and $\varphi = 0°$ on face A of the π-π-rig oriented at $\alpha = 45°$. The thickness of each of the two laminae is $c = 0.25$ mm.

To begin the optimization procedure, construct an 8×5 submatrix composed of transfer matrix elements that couple only the S-polarization of the four modes selected, (0, 0), (−1, 0), (0, −1), and (0, 1). The equations to solve are obtained from Formula (2). The OUT set (DIR,POL,BF) is composed of $(\pm, S, m)$, with $m = 1, \ldots, 4$ from Table 1. Given the absence of any source at $z = +\infty$, the coefficients $C^{\mathrm{DIR}}_{\mathrm{POL,BF}}$ are all zero for $(-, S, m)$, $m = 1, \ldots, 4$. At IN, the set (dir,pol,bf) contains the incoming $(+, S, 1)$ and the reflected $(-, S, m)$, with $m = 1, \ldots, 4$. There are eight unknown coefficients, four at OUT and another four at IN.

The 8×5 matrix transfers the input column vector $(\mathcal{C}^+_{S1}, \mathcal{C}^-_{S1}, \mathcal{C}^-_{S2}, \mathcal{C}^-_{S3}, \mathcal{C}^-_{S4})$ into the output $(C^+_{S1}, C^+_{S2}, C^+_{S3}, C^+_{S4}, 0, 0, 0, 0)$. For ease of reading, the IN and OUT coefficients are marked using distinct fonts. Within this approximation, we can solve eight equations for eight unknown coefficients, by fixing the input $\mathcal{C}^+_{S1} = 1$. The coefficients thus found are the transmission and reflection coefficients for the four modes under consideration.

To construct an objective function for the optimization process we use a series of properties. The first property is that in the vicinity of the resonant frequency the absolute value of the determinant of the 4×4 matrix $(T^{-,-}_{Sm,Sn})$ attains a minimum. The second one is that the absolute values of the transmission and reflection coefficients of the evanescent modes need to attain high values. The third property is based on the absorptance factor defined as $1 - |C^+_{S1}|^2 - |C^+_{S2}|^2 - |\mathcal{C}^-_{S1}|^2 - |\mathcal{C}^-_{S2}|^2$, similar to the definition from [26]. The absorptance factor goes through a maximum around the resonant frequency. The objective function we use is

$$\begin{aligned} &|\mathrm{Det}(T^{-,-}_{Sm,Sn})| + ||C^+_{S1}|^2 + |C^+_{S2}|^2 + |\mathcal{C}^-_{S1}|^2 + |\mathcal{C}^-_{S2}|^2 - 0.5| \\ &\quad + ||C^+_{S3}| - 10| + ||C^+_{S4}| - 10|. \end{aligned} \tag{11}$$

We followed the logic of constructing an objective function analogous to a potential energy composed of the sum of quadratic terms. Furthermore, it is a common practice in numerical optimization procedures to utilize the absolute value of a term instead of its second power, or when the term is a complex number.

Only the transmission coefficients for the evanescent waves are present in Eq. (11) because we expect that the reflection coefficients be very close, in absolute value, to the transmission values. We choose 10 as a target number for this value. For the absorptance factor the target values is chosen at 0.5.

For a fixed frequency in the range of 37–50 GHz, we found a local minimum for this objective function in the six-dimensional space of the dielectric constants, each constant constrained to be between one and 12.

The minimization was completed in minutes using [27]. After scanning 100 frequencies, the local minimum we selected is located at $f = 41.29$ GHz and $\epsilon_{1B} = 4.99$, $\epsilon_{2B} = 2.96$, $\epsilon_{1L} = 7.60$, $\epsilon_{2L} = 5.66$, $\epsilon_{1R} = 5.93$, and $\epsilon_{2R} = 1.63$. At this minimum, $\mathrm{Det}(T^{-,-}_{Sm,Sn}) = 2.5 \times 10^{-5} - 3.7 \times 10^{-5} i$, $C^+_{S1} = 0.59 - 0.0022i$, $\mathcal{C}^-_{S1} = -0.21 - 0.59i$, $C^+_{S2} = 0.041 + 0.31i$, $\mathcal{C}^-_{S2} = 0.04 + 0.34i$, $C^+_{S3} = -10.03 - 0.15i$, $\mathcal{C}^-_{S3} = -10.61 - 0.18i$, $C^+_{S4} = -3.92 + 9.20i$, and $\mathcal{C}^-_{S4} = -4.13 + 9.74i$. We see that the obtained determinant is a small number and that the reflection and the transmission coefficients are close, in absolute value, to the value 10 we imposed. The absorptance factor came out as 0.04, far from the value of 0.5. We included the absorptance in the objective function to observe its deviation from 0.5. This discrepancy was anticipated because, near the resonant frequency, the transmission and reflection coefficients of the propagative modes exhibit minima at slightly different frequencies than the resonance itself.

Technologically, the permittivities at the local minimum point may not be easily implemented, although we constrained the dielectric constants to be less than 12. Instead, below we focus on studying the predictions put forward by the analytic solution and compare them against numerical results from a high-performance software package [25].

These predictions are grouped into three categories. The first category, inspired by topological photonics, is related to robustness of the resonant modes with respect to the change of the dielectric constants, quantified as a map from the real to integer numbers. The second is based on resonant frequency identification, whereas the third is focused on high Q-factors and the use of a complex frequency plane to estimate the Fano-Lorentz spectral line shape for the resonant modes. In what follows we confine ourselves to evanescent S-polarized resonant waves excited by the (0, 0) S-polarized incoming wave.

5. MAP FROM THE REAL TO INTEGER NUMBERS

The resonances in the scattering matrix elements appear as zeroes of the determinant of the $T^{-,-}$ matrix. The minimal $T^{-,-}$ matrix can be reduced to just the matrix element $T^{-,-}_{Sm,Sm}$, presented in Section 9, the zeroes of which give the first approximation for the resonant frequencies. To see that, take a 2×2 transfer matrix built only from the set $T^{\pm,\pm}_{Sm,Sm}$ and look at the resonance for the mode Sm as a singularity for

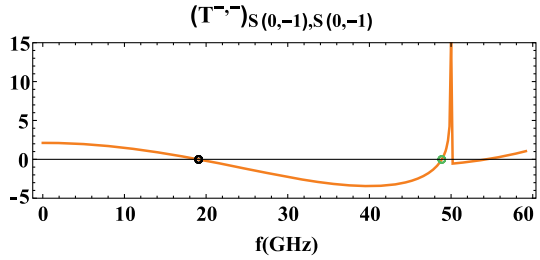

Fig. 2. Theoretical matrix element $T^{-,-}_{S(0,-1),(S(0,-1)}$ as a function of frequency. The zeroes at 19.9 GHz and 48.86 GHz have a negative and a positive slope, respectively. The Rayleigh frequency for the mode $(0, -1)$ is at 50.03 GHz, where a pole singularity is present. The dielectric constants are $\epsilon_{1B} = \epsilon_{2B} = 35$.

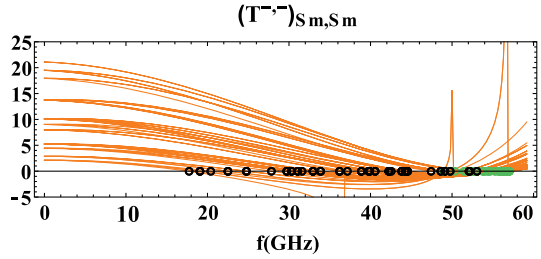

Fig. 3. All matrix elements $T^{-,-}_{Sm,Sm}$ that have at least one zero on the real frequency axis. The zeroes with a negative slope are marked as empty black circles, whereas the zeroes with a positive slope are in green. There are three pole singularities in the range of frequency up to 60 GHz, for $(-1, 0)$, $(0, \pm 1)$ and $(-1, \pm 1)$ at 36.69, 50.03 and 56.71 GHz, respectively.

which Eq. (2) has a non-zero solution if all coefficients but (DIR, POL, BF) = (+, S, m) and (dir, pol, bf) = (−, S, m) are zero. It turns out that this simple approximation has predictive power. As the dielectric constants change their values, the zeroes of $T^{-,-}_{Sm,Sm}$ appear or disappear, creating or destroying a resonance. We study this phenomenon for variable $\epsilon_{1B} = \epsilon_{2B}$, running from one to ∞, with the rest of the dielectric constants kept constant at the optimized values.

Hence, map $\epsilon_{1B} = \epsilon_{1B}$ to the number of modes $m = (M_x, M_y)$ for which the diagonal transfer matrix element $T^{-,-}_{Sm,Sm}$, Section 9, has at least one zero on the frequency axis in the interval [0, 60] GHz:

$$\epsilon \in \mathbb{R} \mapsto \text{number of modes with zeroes.} \qquad \textbf{(12)}$$

The analytic formulas position the zeroes as in Figs. 2 and 3.

As $\epsilon_{1B} = \epsilon_{2B}$ increases from one to ∞, Fig. 4, the number of modes for which $T^{-,-}_{Sm,Sm}$ crosses the real frequency axis increases in discontinuous steps, then decreases as the dielectric constant gets above 30. It reaches a plateau of 36 modes as $\epsilon \to \infty$. Figure 5 shows the position in the (M_x, M_y) plane of the 53 and 36 modes for $\epsilon_{1B} = \epsilon_{2B} = 35$ and ∞, respectively. Two adjacent steps in Fig. 4 have two distinct topological invariants, i.e., distinct number of resonant modes. The boundaries of these steps are not uniformly distributed on the horizontal dielectric axis. Knowing the distribution of these boundary values may play a significant role in assembling compound devices, which are built by bringing together two structures with distinct topological invariants. Numerical simulations, performed via [25],

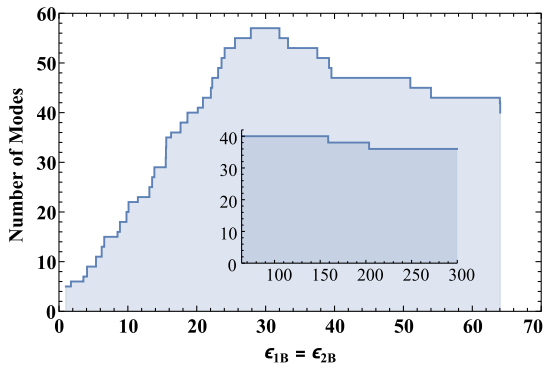

Fig. 4. Topological map of the number of modes $m = (M_x, M_y)$ for which the corresponding diagonal transfer matrix element $T^{-,-}_{Sm,Sm}$ has a zero on the real frequency axis in the interval [0, 60] GHz. The continuous $\epsilon_{1B} = \epsilon_{2B}$ variable runs from one to ∞. The inset's horizontal axis spans 64–300, extending the figure's range of 1–64.

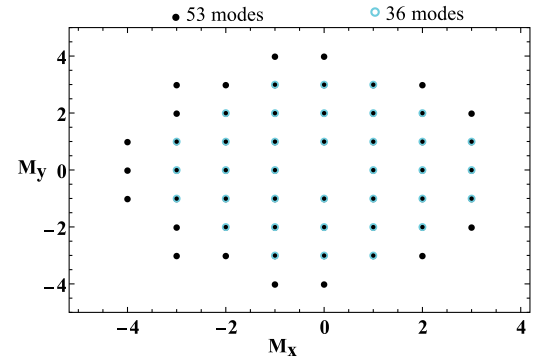

Fig. 5. Modes $m = (M_x, M_y)$. There are 53 modes with a zero on the real frequency axis for $\epsilon_{1B} = \epsilon_{2B} = 35$ and 36 modes for ∞.

confirm that five modes resonate for $\epsilon_{1B} = \epsilon_{2B} = 1$ and 53 for $\epsilon_{1B} = \epsilon_{2B} = 35$.

One step deeper into the analysis of the zeroes is provided by propagation along channels.

A major finding in [18] is that the transfer matrix elements can be expressed as a sum of a small number of terms, which we call channels. Specifically, the computation starts with 729 path operators that transfer the field from the first to the second lamina. Fortunately, many of these path operators come up with a zero contribution and the results of the paths that contribute can be further grouped together in simple terms, which we call channels. Each channel has the interesting attribute of being a product of two terms that bear distinctive features. One term depends on the permittivities, while the other does not. The other term is only dependent on the properties of the excitation wave and the Bloch-Floquet index. Here, we focus on S-polarized resonant surface waves excited by an S-polarized incident field. The transfer of the incident S field into the S output field flows along five channels. The following analysis of the optimization results highlights the value of channel decomposition.

Channel 1 SS does not depend on the dielectric constants and is positive for any frequency and direction $p_\perp$, Fig. 6. Some other channels have to be negative for $T^{-,-}_{Sm,Sm}$ to cross the frequency axis. Interestingly, each channel

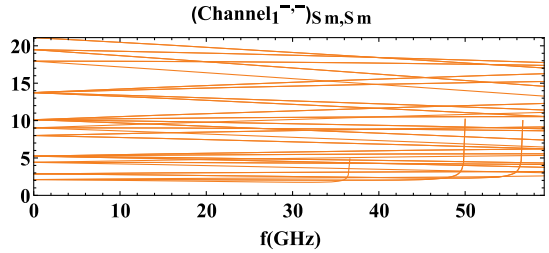

Fig. 6. Channel 1 for all 53 matrix elements $T^{-,-}_{Sm,Sm}$ from Fig. 5. Channel 1 is independent of ϵ.

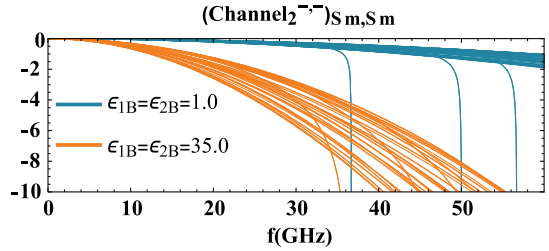

Fig. 7. Channel 2 for all 53 matrix elements $T^{-,-}_{Sm,Sm}$ from Fig. 5, for two values of $\epsilon_{1B} = \epsilon_{2B}$.

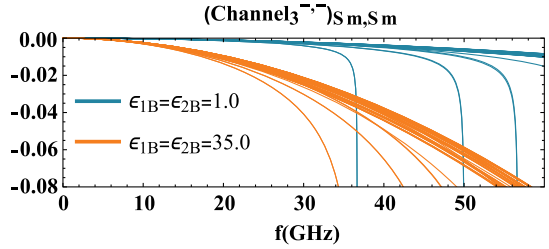

Fig. 8. Channel 3 for all 53 matrix elements $T^{-,-}_{Sm,Sm}$ from Fig. 5, for two values of $\epsilon_{1B} = \epsilon_{2B}$.

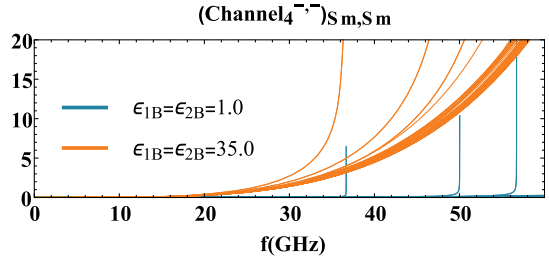

Fig. 9. Channel 4 for all 53 matrix elements $T^{-,-}_{Sm,Sm}$ from Fig. 5, for two values of $\epsilon_{1B} = \epsilon_{2B}$.

keeps a constant sign as a function of frequency, namely, (1, +), (2, −), (3, −), (4, +), and (5, −), noticeable in Figs. 7–10.

From Fig. 8 we see that Channel 3 is two orders of magnitude smaller than the other ones, so it does not lead to creation or destruction of a zero, but contributes to its location on the frequency axis. As $\epsilon_{1B} = \epsilon_{2B}$ increases the negative contribution starts to dominate the positive one and two phenomena appear:

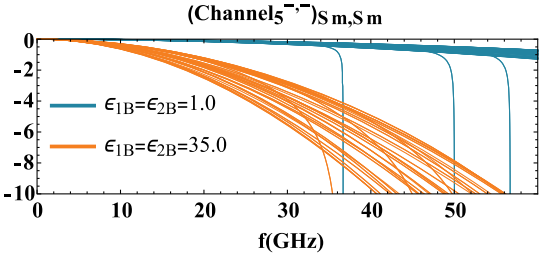

Fig. 10. Channel 5 for all 53 matrix elements $T^{-,-}_{Sm,Sm}$ from Fig. 5, for two values of $\epsilon_{1B} = \epsilon_{2B}$.

Table 2. Variable Layer Width

c [mm]	t	F [GHz]	Ωnum	Ωtheory	Ω%-error
0.100	10	47.540	0.0996365	0.0993646	0.27
0.200	5	43.376	0.181819	0.180396	0.78
0.250	4	41.667	0.218319	0.215294	1.39
0.275	4/11	40.693	0.234537	0.231701	1.21
0.300	10/3	39.908	0.250923	0.247551	1.34

the zeroes are pushed into lower frequencies and a variable number of modes start to cross the frequency axis. This explains the increase in the number of resonant modes as $\epsilon_{1B} = \epsilon_{2B}$ increases.

6. ANALYTICAL PREDICTION OF THE RESONANT FREQUENCY

A. The Thinner the Lamina, the Higher the Precision

From counting the number of zeroes for many modes, we change the focus, Table 2, to predict the position of the zero, Ω_{theory}, of $T^{-,-}_{Sm,Sm}$ for the optimized design modes, $(0, \pm 1)$. Both modes have the same zero at $\varphi = 0°$. The resonant frequency depends on the thickness of the structure's lamina, c. All the other parameters are kept constant.

Notice that $\Omega\%\text{-error} = 100\frac{|\Omega\text{num}-\Omega\text{theory}|}{\Omega\text{num}}$, which measures the distance to the numerical simulation result Ωnum [25], decreases with the decrease of the width c. This is to be expected because as $c \to 0$ the discrete approximation of Maxwell's equations improves.

B. Influence of the Rotation Angle α on the Resonant Frequency

Out of the five channels for transfer of the SS-polarization, only Channels 3 and 4 depend on the angle α. As the angle α is varied, the resonant frequency for the degenerate modes $(0, -1)$ and $(0, 1)$ changes in the vicinity of the frequencies determined at $\alpha = 45°$, Figs. 11 and 12. Although the relative changes are small, with an estimated linear slope of −0.96 MHz/deg and −2.46 MHz/deg, respectively, the slopes are close to the ones from the numerically simulated data. The systematic shift between the theoretical and numerical values, described for $\alpha = 45°$ in Table 2, is the same for all angles α.

The study of the wedge effect, which comes out for $0° < \alpha < 10°$ or for $80° < \alpha < 90°$, will be covered in a different manuscript.

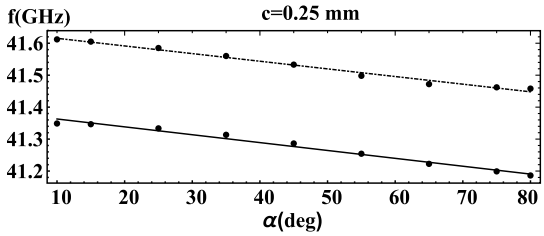

Fig. 11. Resonant frequency of the modes $S(0, -1)$ and $S(0, 1)$ as a function of α. The dotted-dashed line corresponds to the numerical data, whereas the continuum line to the analytical transfer matrix.

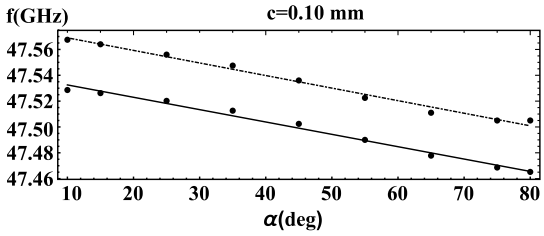

Fig. 12. Resonant frequency of the modes $S(0, -1)$ and $S(0, 1)$ as a function of α. The dotted-dashed line corresponds to the numerical data, whereas the continuum line to the analytical transfer matrix.

7. HIGH Q-FACTOR BILAMINAR STRUCTURE

To study the theoretical prediction for the amplitude we choose a series of resonances with large Q-factors. The first has $Q = 4.8 \times 10^6$ at -3 dB, Fig. 13. The theoretical values were computed using a 20×20 transfer matrix. Two systematic shifts, f_{shift} and t_{shift}, are needed to superpose the theoretical formula $20 \log_{10} |t^{\max,\min}_{S(0,1),S(0,0)}(f - f_{\text{shift}})| + t_{\text{shift}}$ on numerical simulations. For Fig. 13, $f_{\text{shift}} = 3.2\,10^{-5}$GHz and $t_{\text{shift}} = -3.9$ dB. The lamina being thin, $c = 0.01$ mm, the shifts are small with respect to the frequency and amplitude at resonance.

Variable φ offers another venue to study the amplitude around a high Q-factor resonance. The modes $(0, -1)$ and $(0,1)$ are degenerate for $\varphi = 0°$, having the same Rayleigh and resonant frequency. As the angle φ slides away from 0°, the scattering amplitude of the mode $S(0, -1)$ decreases, whereas

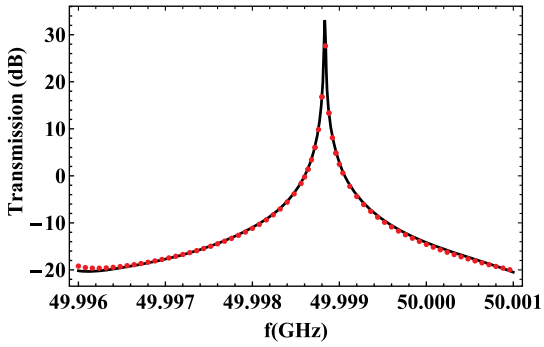

Fig. 13. Resonance with a high Q-factor. The Q-factor at -3 dB is $Q = 4.8 \times 10^6$. The black curve represents the theoretical transmission from $S(0, 0)$ at z- min to $S(0, 1)$ at z- max. The red points were numerically simulated via [25]. All parameters are equal to the optimized values except for $c = 0.01$ mm and $\epsilon_{2R} = 1.0$.

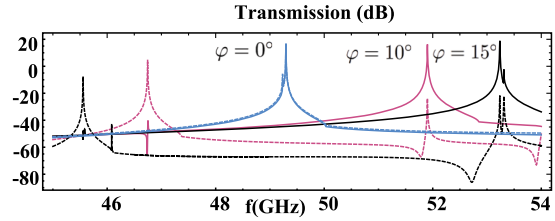

Fig. 14. Resonances with a high Q-factor for variable incident angle φ. The parameters are $c = 0.05$ mm and $\varphi = 0°$, 10°, and 15°. All the other parameters are placed at the optimized values. The continuous and dashed curves represent the theoretical transmission from $S(0, 0)$ at z- min to $S(0, 1)$ and $S(0, -1)$ at z- max, respectively. For $\varphi = 0°$, 10° and $\varphi = 15°$, the resonant frequency, in GHz, and the Q-factors are $(49.30, 3.6 \times 10^4)$, $(51.90, 5.2\,10^3)$, and $(53.24, 1.3\,10^4)$, respectively.

Table 3. Variable c for $\varphi = 15°$[a]

c [mm]	f_{shift}	t_{shift}	Q
0.25	$3.2\,10^{-1}$	9.81	$1.1\,10^3$
0.10	$5.4\,10^{-2}$	5.67	$2.6\,10^3$
0.05	$9.4\,10^{-3}$	2.85	$1.3\,10^4$
0.01	$9.0\,10^{-5}$	−3.78	$1.2\,10^6$

[a]Scattering matrix element for input $S(0, 0)$ at z-min output $S(0, 1)$ at z-max. Frequency shifts are measured in GHz and the amplitude of shifts of the scattering matrix elements in dB.

the scattering amplitude for the mode $S(0, 1)$ remains excited at high dB levels, Fig. 14.

The same trend was confirmed by numerical simulation. Table 3 contains additional data for the comparison between theory and numerical simulations for the high Q-factors.

8. COMPLEX-FREQUENCY PLANE AND THE WEIGHTED FANO-LORENTZ LINE SHAPE

Moving beyond predicting the position of the resonant frequency and its amplitude, the complete analytical solution for the transfer matrix provides a simple but meaningful approximation for the resonant line shape:

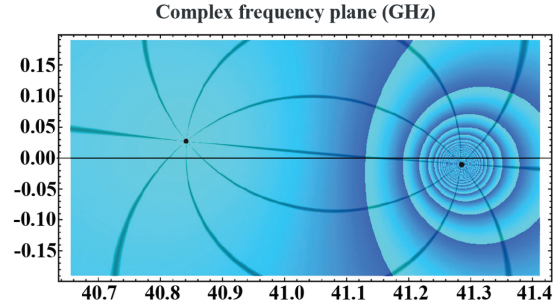

Fig. 15. Representation, in the complex frequency plane, of the scattering matrix element Out $S(0, 1)$ at z-min, In $S(0, 0)$ at z-max. The closed curves around the pole $41.286 - i0.009$ show the absolute value of the scattering matrix as it tends to infinity. The argument of the scattering matrix element is constant on the curves that connect the zero at $40.843 + 0.027\,i$ with the pole. The real resonant frequency is located above the pole, at 41.286 GHz.

$$t^{\min,\max}_{S(0,1),S(0,0)} = \frac{\text{Cofactor}_{S(0,0),S(0,1)}(T^{-,-})}{\text{Det}(T^{-,-})} \cong \rho e^{i\Phi}\frac{f-f_{\text{zero}}}{f-f_{\text{pole}}}. \tag{13}$$

Here $t^{\min,\max}_{S(0,1),S(0,0)}$ is the scattering matrix element, which describes the transmission of the mode $S(0, 0)$ from z-max, i.e., located at $z > 0$, into the mode $S(0, 1)$ from z-min, i.e., located at $z < 0$. The zero and the pole from Eq. (13) are located in the complex frequency plane, both in the vicinity of the real resonant frequency [24]. The meromorphic approximation, Eq. (13), has a natural structure of dipoles with the monopoles placed at f_{zero} and f_{pole}, Fig. 15.

The zero-pole model, extracted from a 20×20 matrix $t^{\min,\max}$, is

$$t^{\min,\max}_{S(0,1),S(0,0)} = 0.053\, e^{-2.732i}\,\frac{f-f_{\text{zero}}}{f-f_{\text{pole}}}, \tag{14}$$

with frequency, in GHz, given by

$$f_{\text{zero}} = 40.843 + 0.027i,\ f_{\text{pole}} = 41.286 - 0.009i.$$

Following [24], we express the scattering line shape $|t^{\min,\max}_{S(0,1),S(0,0)}|^2$ in different forms. The first is

$$\begin{aligned}|t^{\min,\max}_{S(0,1),S(0,0)}|^2(x) &= \rho^2\frac{(\delta+x)^2+\gamma^2}{1+x^2}\\ &= 2.81\times10^{-3}\frac{(-47.47+x)^2+8.55}{1+x^2},\end{aligned} \tag{15}$$

where $x = -\frac{f-\text{Re}(f_{\text{pole}})}{\text{Im}(f_{\text{pole}})}$, $\delta = -\frac{\text{Re}(f_{\text{pole}}-f_{\text{zero}})}{\text{Im}(f_{\text{pole}})}$, and $\gamma = \frac{\text{Im}(f_{\text{zero}})}{\text{Im}(f_{\text{pole}})}$. The second form is connected with the presence of a continuum background:

$$|t^{\min,\max}_{S(0,1),S(0,0)}|^2(x) = A_0 + F_0\frac{(\nu+x)^2}{1+x^2}. \tag{16}$$

We found two solutions for the parameters A_0, F_0, and ν, namely, $A_0 = 1.06\times10^{-5}$, $F_0 = 2.8\times10^{-3}$, and $\nu = -47.65$, or $A_0 = 6.37$, $F_0 = -6.36$, and $\nu = 2.09\times10^{-2}$. This form is thus ambiguous as is also noted in [24].

The third, and final, format presents the resonant line shape as a weighted sum of a Fano and Lorentz line shapes:

$$|t^{\min,\max}_{S(0,1),S(0,0)}|^2(x) = A\left(\eta\frac{(\delta+x)^2}{1+x^2} + (1-\eta)\frac{1}{1+x^2}\right), \tag{17}$$

where the weight parameter is $\eta = 1/(1+\gamma^2) = 0.105$ and $A = \rho^2(1+\gamma^2) = 0.027$.

The Fano line shape, which is the first term in Eq. (17), contributes 10.5% to the resonance line shape.

9. DIAGONAL $T^{-,-}_{Sm,Sm}$ MATRIX ELEMENTS FOR THE π-π-RIG

Here is the list of the five channels through which the S-polarized electromagnetic field is transferred. The parameters are

$$p_x^{\text{IN/OUT}} = 2\pi\frac{M_x^{\text{IN/OUT}}}{l_x} + \Omega\sin(\theta)\cos(\varphi), \tag{18}$$

$$p_y^{\text{IN/OUT}} = 2\pi\frac{M_y\,\text{IN/OUT}}{l_y} + \Omega\sin(\theta)\sin(\varphi), \tag{19}$$

where l_x and l_y are the c-scaled dimensions of the unit cell, (M_x, M_y) is the Bloch-Floquet mode number, Ω is the c-scaled frequency, and (θ, φ) is the direction of the $(0, 0)$ mode.

From the dispersion relation of the Pendry-MacKinnon discrete electrodynamics, we can see that for both IN and OUT the p_z component appears in $\varphi_z = e^{ic p_z}$, where $\varphi_z(\zeta) = \zeta - \sqrt{|\zeta^2-1|}e^{\frac{i}{2}(\arg(\zeta-1)+\arg(\zeta+1))}$. The $\arg(\zeta)$ takes values on $[-\pi, \pi)$ in such a way that $\arg(\zeta) = -\pi$ if $\text{Im}(\zeta) = 0$ and $\zeta < 0$. The argument ζ is defined as $\zeta = 1 - \frac{\Omega^2}{2} + \frac{c^2}{2}(p_x^2 + p_y^2)$.

For simplicity, p_x^{IN} below appears as p_x. Although for the diagonal matrix elements $\varphi_z(\zeta^{\text{IN}}) = \varphi_z(\zeta^{\text{OUT}})$, the IN and OUT indices are retained in the argument to show the origin of these terms:

$$(T^{-,-}_{Sm,Sm})_{\text{Channel 1}} = -\delta_{\text{IN,OUT}}\frac{\left((\Omega^2\varphi_{z,\text{OUT}}+1)^2 - (\varphi_{z,\text{OUT}})^2\right)}{\left(\varphi^2_{z,\text{OUT}}-1\right)\varphi^3_{z,\text{OUT}}}, \tag{20}$$

$$(T^{-,-}_{Sm,Sm})_{\text{Channel 2}} = (6\epsilon_{1B} + \epsilon_{1L} + \epsilon_{1R})\,\frac{\Omega^2\left(\Omega^2\varphi_{z,\text{OUT}} + 1\right)}{8\varphi_{z,\text{IN}}\left(\varphi^2_{z,\text{OUT}} - 1\right)\varphi_{z,\text{OUT}}}, \tag{21}$$

$$\begin{aligned}
(T^{-,-}_{Sm,Sm})_{\text{Channel 3}} = {} & \frac{\Omega^2}{4\pi^2 t^2\left(p_x^2 + p_y^2\right)\varphi_{z,\text{IN}}\left(\varphi^2_{z,\text{OUT}} - 1\right)} \\
& \times \left(p_x^2\left(\csc(\alpha)\sec(\alpha)\epsilon_{2B}\left(2\ln(\epsilon_{1B}) - \ln(\epsilon_{1L}) - \ln(\epsilon_{1R})\right)\right.\right. \\
& + \epsilon_{2L}\left(-\csc(\alpha)\sec(\alpha)\log(\epsilon_{1B}) + \frac{3\csc(\alpha)\log(\epsilon_{1L})}{2(\sin(\alpha)+\cos(\alpha))} - \frac{(\cot(\alpha)-2)\csc(\alpha)\sec(\alpha)\log(\epsilon_{1R})}{2(\cot(\alpha)+1)}\right) \\
& \left. + \epsilon_{2R}\left(-\csc(\alpha)\sec(\alpha)\log(\epsilon_{1B}) - \frac{(\cot(\alpha)-2)\csc(\alpha)\sec(\alpha)\log(\epsilon_{1L})}{2(\cot(\alpha)+1)} + \frac{3\csc(\alpha)\log(\epsilon_{1R})}{2(\sin(\alpha)+\cos(\alpha))}\right)\right) \\
& + p_x p_y \frac{\csc(\alpha)}{\sin(\alpha)+\cos(\alpha)}\left(\epsilon_{2L} - \epsilon_{2R}\right)\left(\log(\epsilon_{1L}) - \log(\epsilon_{1R})\right) \\
& + p_y^2\left(\csc(\alpha)\sec(\alpha)\epsilon_{2B}\left(2\log(\epsilon_{1B}) - \log(\epsilon_{1L}) - \log(\epsilon_{1R})\right)\right. \\
& + \epsilon_{2L}\left(-\csc(\alpha)\sec(\alpha)\log(\epsilon_{1B}) + \frac{(3\cot(\alpha)+2)\csc(\alpha)\sec(\alpha)\log(\epsilon_{1L})}{2(\cot(\alpha)+1)} - \frac{\csc(\alpha)\log(\epsilon_{1R})}{2(\sin(\alpha)+\cos(\alpha))}\right) \\
& \left.\left. + \epsilon_{2R}\left(-\csc(\alpha)\sec(\alpha)\log(\epsilon_{1B}) - \frac{\csc(\alpha)\log(\epsilon_{1L})}{2(\sin(\alpha)+\cos(\alpha))} + \frac{(3\cot(\alpha)+2)\csc(\alpha)\sec(\alpha)\log(\epsilon_{1R})}{2(\cot(\alpha)+1)}\right)\right)\right),
\end{aligned} \tag{22}$$

$$\begin{aligned}
(T^{-,-}_{Sm,Sm})_{\text{Channel 4}} = {} & -\frac{\Omega^4}{128\varphi_{z,\text{IN}}\left(\varphi^2_{z,\text{OUT}} - 1\right)} \\
& (64\epsilon_{1B}\epsilon_{2B} + 16\epsilon_{1B}\epsilon_{2L} + 16\epsilon_{1B}\epsilon_{2R} + 16\epsilon_{2B}\epsilon_{1L} + 16\epsilon_{2B}\epsilon_{1R} + \frac{4(\cos(\alpha) - \sin(\alpha))}{\sin(\alpha)+\cos(\alpha)} \\
& \csc^2\left(\frac{1}{4}(2\alpha+\pi)\right)\sec(\alpha)(2\sin(\alpha)\left(\epsilon_{1L} - \epsilon_{1R}\right)\left(\epsilon_{2L} - \epsilon_{2R}\right) + \cos(2\alpha) + 3)\left(\epsilon_{1B} - \epsilon_{1R}\right)\left(\epsilon_{2B} - \epsilon_{2L}\right) \\
& - 4\cot(\alpha)\cot^2\left(\frac{1}{4}(2\alpha+\pi)\right)\left(\epsilon_{1B} - \epsilon_{1L}\right)\left(\epsilon_{2B} - \epsilon_{2L}\right) \\
& + \csc^2\left(\frac{1}{4}(2\alpha+\pi)\right)\sec(\alpha)(2\sin(\alpha) + \cos(2\alpha) + 3)\left(\epsilon_{1B} - \epsilon_{1L}\right)\left(\epsilon_{2B} - \epsilon_{2R}\right) \\
& - 4\cot(\alpha)\cot^2\left(\frac{1}{4}(2\alpha+\pi)\right)\left(\epsilon_{1B} - \epsilon_{1R}\right)\left(\epsilon_{2B} - \epsilon_{2R}\right) \\
& 4\left(2\tan\left(\frac{\alpha}{2}\right) + \cot(\alpha)\right)\left(\left(\epsilon_{1B} - \epsilon_{1L}\right)\left(\epsilon_{2B} - \epsilon_{2L}\right) + \left(\epsilon_{1B} - \epsilon_{1R}\right)\left(\epsilon_{2B} - \epsilon_{2R}\right)\right) \\
& - 4\tan^2\left(\frac{\alpha}{2}\right)\tan(\alpha)\left(\left(\epsilon_{1B} - \epsilon_{1L}\right)\left(\epsilon_{2B} - \epsilon_{2L}\right) + \left(\epsilon_{1B} - \epsilon_{1R}\right)\left(\epsilon_{2B} - \epsilon_{2R}\right)\right)),
\end{aligned} \tag{23}$$

$$(T^{-,-}_{Sm,Sm})_{\text{Channel 5}} = (6\epsilon_{2B} + \epsilon_{2L} + \epsilon_{2R})\,\frac{\Omega^2\left(\Omega^2\varphi_{z,\text{IN}} + 1\right)}{8\varphi^2_{z,\text{IN}}\left(\varphi_{z,\text{OUT}} - 1\right)\left(\varphi_{z,\text{OUT}} + 1\right)}. \tag{24}$$

10. CONCLUSION

To sum up, we show that the transfer matrix obtained from Pendry-MacKinnon's discrete Maxwell's equations is extremely useful for inverse design. Having access to a closed-form analytical solution for any polygonal-patterned bilaminar structure allows for rapid and accurate design and analysis of these structures, compared to iterative optimization.

A valuable way to proceed further is to extend the range of applications of this work. One possibility is to exploit Fig. 4 and bring together two devices with distinct numbers of resonant modes. This would allow for the examination of propagation along different channels at the interface. Other potential applications include metasurfaces [28], energy harvesting [29–31], leaky-wave theory [31], and frequency-selective surfaces [32].

Acknowledgment. O.L. wishes to thank the Fulbright Commission for a Fulbright Scholarship grant and the host Victor Lopez-Richard from Universidade Federal de São Carlos, SP, Brazil, where part of this work was done. In addition, O.L. thanks his colleague Mariama Rebello de Sousa Dias for many conversations during the course of this research. Both of us wish to thank Dr. Andrei Silaghi, with Continental Automotive Romania SRL, for facilitating the access to numerical simulation using CST Microwave Studio [25].

Disclosures. The authors declare no conflicts of interest.

Data availability. Data underlying the results presented in this paper are not publicly available at this time but may be obtained from the authors upon reasonable request.

REFERENCES

1. J. Xiong, E.-L. Hsiang, Z. He, *et al.*, "Augmented reality and virtual reality displays: emerging technologies and future perspectives," Light Sci. Appl. **10**, 1 (2021).
2. B. C. Kress and I. Chatterjee, "Waveguide combiners for mixed reality headsets: a nanophotonics design perspective," Nanophotonics **10**, 41–74 (2021).
3. N. Shlezinger, G. C. Alexandropoulos, M. F. Imani, *et al.*, "Dynamic metasurface antennas for 6g extreme massive MIMO communications," IEEE Wireless Commun. **28**, 106–113 (2021).
4. J. Lorenzo, A. Lázaro, R. Villarino, *et al.*, "Modulated frequency selective surfaces for wearable RFID and sensor applications," IEEE Trans. Antennas Propag. **64**, 4447–4456 (2016).
5. E. Descrovi, T. Sfez, M. Quaglio, *et al.*, "Guided Bloch surface waves on ultrathin polymeric ridges," Nano Lett. **10**, 2087–2091 (2010).
6. P. Lova, G. Manfredi, and D. Comoretto, "Advances in functional solution processed planar 1d photonic crystals," Adv. Opt. Mater. **6**, 1800730 (2018).
7. T. Feichtner, O. Selig, M. Kiunke, *et al.*, "Evolutionary optimization of optical antennas," Phys. Rev. Lett. **109**, 127701 (2012).
8. S. Mertens, "Random costs in combinatorial optimization," Phys. Rev. Lett. **84**, 1347 (2000).
9. L. L. Sánchez-Soto, J. J. Monzón, A. G. Barriuso, *et al.*, "The transfer matrix: a geometrical perspective," Phys. Rep. **513**, 191–227 (2012).
10. S. F. Koufidis and M. W. McCall, "Möbius transformation and coupled-wave theory: complete identification of the transfer matrix," Phys. Rev. A **106**, 062213 (2022).
11. D. Rhazi and N. Atalla, "A simple method to account for size effects in the transfer matrix method," J. Acoust. Soc. Am. **127**, EL30–EL36 (2010).
12. Z.-Y. Li and L.-L. Lin, "Photonic band structures solved by a plane-wave-based transfer-matrix method," Phys. Rev. E **67**, 046607 (2003).
13. Y. Khorrami, D. Fathi, and R. C. Rumpf, "Guided-mode resonance filter optimal inverse design using one-and two-dimensional grating," J. Opt. Soc. Am. B **37**, 425–432 (2020).
14. Y. Khorrami, D. Fathi, and R. C. Rumpf, "Fast optimal design of optical components using the cultural algorithm," Opt. Express **28**, 15954–15968 (2020).
15. Y. Khorrami and D. Fathi, "Broadband thermophotovoltaic emitter using magnetic polaritons based on optimized one-and two-dimensional multilayer structures," J. Opt. Soc. Am. B **36**, 662–666 (2019).
16. Y. Khorrami, D. Fathi, A. Khavasi, *et al.*, "Dynamical control of multilayer spacetime structures using extended Fourier modal method," IEEE Photonics J. **13**, 5000110 (2021).
17. Y. Khorrami, D. Fathi, A. Khavasi, *et al.*, "From asymmetrical transmitter to the nonreciprocal isolator using time-varying metasurfaces," Opt. Quantum Electron. **54**, 268 (2022).
18. O.-Z. Lipan and A. De Sabata, "Closed-form analytical solution for the transfer matrix based on Pendry-Mackinnon discrete Maxwell's equations," arXiv, arXiv:2303.06765 (2023).
19. J. Pendry and A. MacKinnon, "Calculation of photon dispersion relations," Phys. Rev. Lett. **69**, 2772 (1992).
20. J. Pendry, "Photonic band structures," J. Mod. Opt. **41**, 209–229 (1994).
21. J. Pendry and P. Bell, "Transfer matrix techniques for electromagnetic waves," in *Photonic Band Gap Materials* (Springer, 1996), pp. 203–228.
22. C. E. J. Png and Y. Akimov, *Nanophotonics and Plasmonics: An Integrated View* (CRC Press, 2017).
23. U. Fano, "Sullo spettro di assorbimento dei gas nobili presso il limite dello spettro d'arco," Il Nuovo Cimento (1924-1942) **12**, 154–161 (1935).
24. I. Avrutsky, R. Gibson, J. Sears, *et al.*, "Linear systems approach to describing and classifying Fano resonances," Phys. Rev. B **87**, 125118 (2013).
25. CST, "Computer Simulation Technology," v2022 (2022).
26. J. Polo, T. Mackay, and A. Lakhtakia, *Electromagnetic Surface Waves: A Modern Perspective* (Newnes, 2013).
27. W. R. Inc., "Mathematica, Version 13.0," Champaign, IL, 2021.
28. M. Barbuto, Z. Hamzavi-Zarghani, M. Longhi, *et al.*, "Metasurfaces 3.0: a new paradigm for enabling smart electromagnetic environments," IEEE Trans. Antennas Propag. **70**, 8883–8897 (2021).
29. J. Zhou, P. Zhang, J. Han, *et al.*, "Metamaterials and metasurfaces for wireless power transfer and energy harvesting," Proc. IEEE **110**, 31–55 (2021).
30. H. A. Atwater and A. Polman, "Plasmonics for improved photovoltaic devices," Nat. Mater. **9**, 205–213 (2010).
31. A. A. Eteng, H. H. Goh, S. K. A. Rahim, *et al.*, "A review of metasurfaces for microwave energy transmission and harvesting in wireless powered networks," IEEE Access **9**, 27518–27539 (2021).
32. D. Ferreira, R. F. Caldeirinha, I. Cuinas, *et al.*, "A review of manufacturing materials and production methods for frequency-selective structures [wireless corner]," IEEE Antennas Propag. Mag. **60**(6), 110–119 (2018).